Research Square

Preprints are preliminary reports that have not undergone peer review.
They should not be considered conclusive, used to inform clinical practice,
or referenced by the media as validated information.

Photothermal nanomodulated GelMA-g-PNIPAM hydrogel for near-infrared remote regulation of drug release

Zehua Jiao
Sichuan University
Tong Shao
Sichuan University
Fanying Zeng
Sichuan University
Shaojian Lin
Sichuan University
Jianwu Lan
Sichuan University
Guolin He
Sichuan University
Jiaojiao Shang
jiaoj.shang@scu.edu.cn

Sichuan University https://orcid.org/0000-0003-2110-7299

Research Article

Keywords: GelMA-g-PNIPAM, thermoresponsive polymer network, Prussian blue nanoparticles, photothermal regulation, nanoparticle–polymer interface, controlled drug release

Posted Date: November 25th, 2026

DOI: https://doi.org/10.21203/rs.3.rs-11851467/v1

License: This work is licensed under a Creative Commons Attribution 4.0 International License.
Read Full License

Additional Declarations: The authors declare no competing interests.

Photothermal nanomodulated GelMA-g-PNIPAM hydrogel for near-infrared remote regulation of drug release

Zehua Jiao[1], Tong Shao[1] , Fanying Zeng[3], Shaojian Lin[1], Jianwu Lan[1], Guolin He[3]*, Jiaojiao Shang[1,2,*]

[1]College of Biomass Science and Engineering, Sichuan University, Chengdu, Sichuan 610065, China.

[2]National Engineering Laboratory for Clean Technology of Leather Manufacture, Sichuan University, Chengdu, Sichuan 610065, China.

[3]Laboratory of the Key Perinatal Diseases, Key Laboratory of Birth Defects and Related Diseases of Women and Children, Ministry of Education, Department of Obstetrics and Gynecology, West China Second University Hospital, Sichuan University, Chengdu, Sichuan Province, China

*Corresponding author: jiaoj.shang@scu.edu.cn (J.S.); heguolin19@163.com

Abstract: Remotely regulating drug release from thermoresponsive polymer networks requires an effective strategy for converting external stimuli into localized thermal signals. Herein, a photothermally regulated GelMA-g-PNIPAM hydrogel was constructed by integrating tannic acid-modified Prussian blue nanoparticles (TA@PB) into a PNIPAM-grafted gelatin methacryloyl network. PNIPAM grafting introduced a reversible thermal transition, while TA@PB nanoparticles provided stable near-infrared (NIR) photothermal conversion under 808 nm irradiation. The resulting hydrogel exhibited temperature-dependent swelling and drug-release behavior, with cumulative amoxicillin release increasing from 42.57% at 25 °C to 92.61% at 40 °C after 3 days. More importantly, cyclic NIR irradiation produced corresponding changes in the release profile, demonstrating remote photothermal regulation of drug release through the thermoresponsive transition of PNIPAM segments. Structural characterization further showed that PNIPAM grafting altered the porous architecture of the gelatin-based network, while TA@PB was homogeneously incorporated without substantially changing the overall porosity. These results establish a nanoparticle–polymer coupling strategy that converts external optical stimulation into thermoresponsive polymer transitions for remote regulation of drug release.

Keywords: GelMA-g-PNIPAM; thermoresponsive polymer network; Prussian blue nanoparticles; photothermal regulation; nanoparticle–polymer interface; controlled drug release

1. Introduction

Stimuli-responsive polymer networks provide an effective means of regulating molecular transport through reversible changes in chain conformation, network hydration, and permeability [1–7]. Among the different modes of external regulation, thermal stimulation is particularly attractive because temperature-dependent polymer transitions can directly alter the diffusion environment within a network. However, conventional thermal regulation generally relies on changes in the bulk environmental temperature, making localized and remotely addressable control difficult [8]. Developing polymer systems that can translate an external energy input into a localized and reversible thermal response is therefore important for the controlled regulation of network behavior and drug release [9–13].

Hydrogels are well suited for constructing responsive polymer systems because their hydrated three-dimensional networks can accommodate both functional polymer segments and dispersed nanocomponents [14–16]. Gelatin methacryloyl (GelMA) is an attractive matrix for this purpose because methacryloyl modification provides reactive sites for polymer-network construction while retaining the inherent characteristics of gelatin [17–21]. Nevertheless, conventional GelMA networks exhibit limited structural adaptability after formation, and drug transport is predominantly governed by passive diffusion through relatively fixed hydrated networks [8,22]. Introducing dynamic polymer segments into GelMA therefore provides a route to impart reversible structural responsiveness and regulate drug release through changes in polymer-chain conformation [3,23].

Poly(N-isopropylacrylamide) (PNIPAM) is a representative thermoresponsive polymer that undergoes a reversible hydration–dehydration transition near its lower critical solution temperature (LCST) [23,24]. Below the LCST, PNIPAM chains remain hydrated and expanded, whereas heating above the LCST induces dehydration and chain contraction, thereby altering network hydration and molecular accessibility [1,25]. These conformational changes provide a molecular basis for regulating diffusion and drug release from thermoresponsive polymer networks [3,22,26]. Grafting PNIPAM onto a GelMA backbone can therefore introduce temperature-dependent structural adaptability into the gelatin-derived network [27–29]. However, the PNIPAM transition itself does not provide spatial or remote control; practical regulation still requires a localized and externally addressable thermal input [30,31].

Photothermal nanomaterials provide an effective means of supplying such

localized thermal stimulation by converting optical energy into heat [30,32,33]. Prussian blue (PB) nanoparticles are particularly attractive because of their strong NIR absorption, photothermal conversion capability, and chemical stability [34,35]. The feasibility of coupling PB with PNIPAM has already been demonstrated; for example, Pelluau et al. incorporated PB nanoparticles into a PNIPAM-based hydrogel and achieved NIR-induced shape change and fluorescein release [36]. This work established that PB-mediated photothermal heating can actuate the PNIPAM volume transition. However, the existence of this general mechanism does not by itself ensure effective integration into a gelatin-derived graft polymer network, where nanoparticle dispersion, polymer–particle interactions, and the resulting drug-release response depend strongly on the material architecture and interface design.

Effective photothermal regulation also depends on the homogeneous incorporation of nanoparticles within the polymer matrix. Inorganic nanoparticles frequently undergo aggregation or heterogeneous distribution in polymer networks, which can lead to spatially nonuniform photothermal responses and weaken nanoparticle–polymer coupling [37–40]. Surface functionalization provides a practical approach to improve nanoparticle dispersion and modify interfacial interactions [41]. More generally, surface chemistry, electrostatic interactions, and hydrophobicity are known to influence molecular adsorption and organization at functionalized inorganic interfaces [42,43]. Tannic acid (TA), a polyphenolic molecule containing abundant phenolic hydroxyl groups, can interact with metal-containing surfaces through coordination and hydrogen-bonding interactions [44,45]. Modification of PB with TA may therefore facilitate its dispersion and incorporation within the GelMA-g-PNIPAM network, allowing photothermal conversion to be more effectively coupled with the thermoresponsive polymer transition.

Herein, we construct a photothermally regulated GelMA-g-PNIPAM hydrogel by incorporating TA-modified PB nanoparticles into a PNIPAM-grafted gelatin methacryloyl network. In this design, the GelMA-g-PNIPAM architecture provides a reversible thermoresponsive transition, whereas TA@PB converts 808 nm NIR irradiation into localized heat to actuate the PNIPAM response. The effects of PNIPAM grafting and TA@PB incorporation on polymer structure, porous architecture, swelling behavior, and photothermal performance were systematically investigated. Particular emphasis was placed on determining whether NIR irradiation could be translated into controllable changes in drug release through photothermal activation of the PNIPAM

transition. The overall fabrication and photothermal regulation strategy is illustrated in Scheme 1. This work therefore establishes a nanoparticle–polymer coupling approach for remotely regulating drug release from thermoresponsive polymer networks.

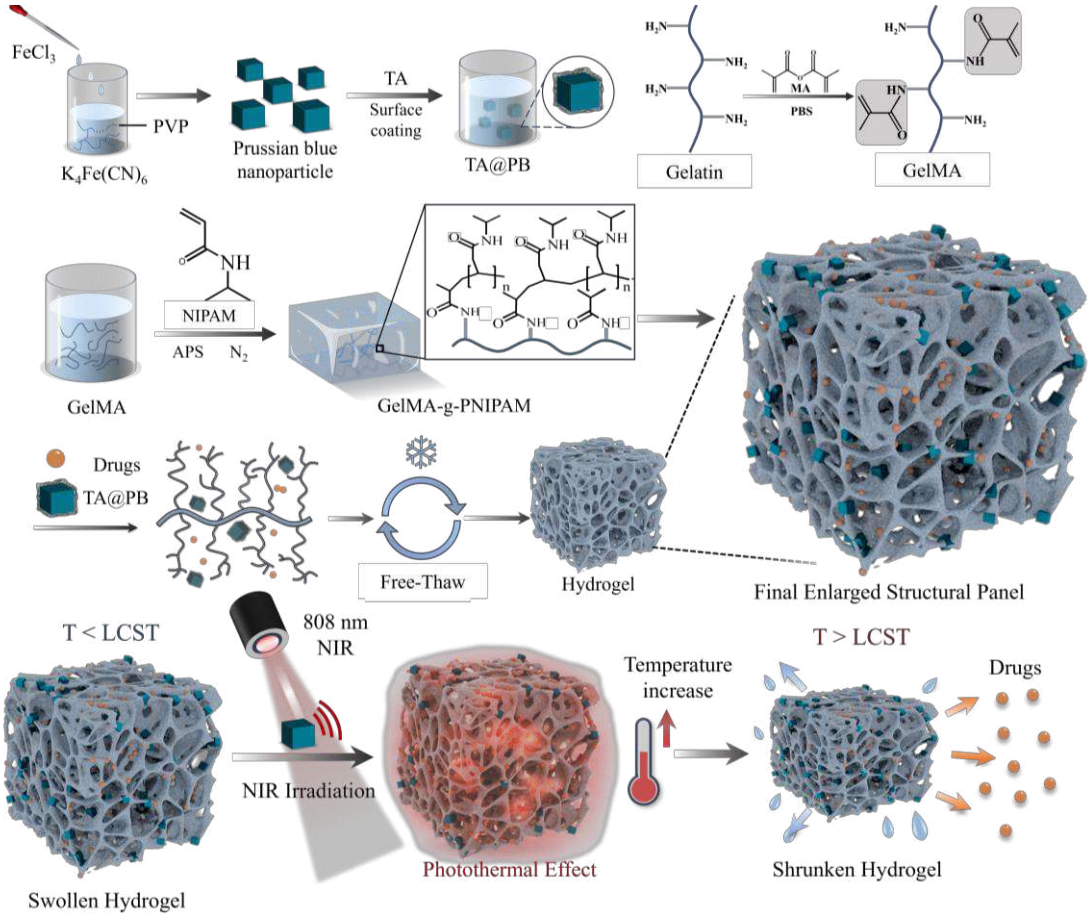

Scheme 1. Schematic illustration of the fabrication and NIR-triggered drug-release mechanism of the TA@PB-containing GelMA-g-PNIPAM hydrogel.

2. Materials and methods

2.1 Materials

Gelatin, Tannic Acid (analytical grade, ≥99%) and N,N,N',N'-Tetramethylethylenediamine (analytical grade, ≥99%) were obtained from Adamas-beta Reagent Co., Ltd. (Shanghai, China). Poly(ethylene glycol) diacrylate, Potassium ferrocyanide trihydrate ($K_4FeC_6N_6·3H_2O$) (analytical grade, ≥99%) and Methacrylic anhydride (analytical grade, ≥94%, contains 0.2% topanol stabilizer) were supplied by Shanghai Aladdin Biochemical Technology Co., Ltd. Polyvinylpyrrolidone K30, Iron(III) chloride hexahydrate ($FeCl_3·6H_2O$) and Ammonium persulfate were obtained from Chengdu Kelong Chemicals Co., Ltd. Amoxicillin (AMX) was purchased from

Macklin Biochemical Co., Ltd. (Shanghai, China). Deionized (DI) water was utilized throughout the experiments.

2.2 Preparation of TA-Modified Prussian Blue Nanoparticles

TA@PB was synthesized through a facile in situ metal–phenolic coating process. Briefly, Prussian Blue nanoparticles were first generated by the controlled dropwise addition of $FeCl_3$ (0.01 M) into a $K_4[Fe(CN)_6]$ solution (0.01 M) containing PVP under continuous stirring. After reaction at room temperature for 3 h, a homogeneous PB nanoparticle dispersion was obtained. Subsequently, tannic acid solution (10 mL, 2.5 mg/mL) was introduced into the PB dispersion and allowed to react for an additional 4 h under mild stirring.Three formulations with nominal TA/PB feed mass ratios of 2:1, 1:1, and 1:2 were prepared by adjusting the relative amounts of TA and PB, and were designated TA@PB-1, TA@PB-2, and TA@PB-3, respectively. TA@PB-2 was selected for subsequent experiments. The comparative characterization of the three formulations is presented in Section 3.1 and 3.2. Owing to the strong affinity between phenolic hydroxyl groups and the Fe^{3+} and $Fe^{2+}$from PB surface, TA was spontaneously deposited onto the PB nanoparticle surface, generating a stable metal–phenolic interfacial coating. The resulting TA@PB nanoparticles were then purified by microporous membrane filtration to remove unbound molecules and stored in aqueous dispersion for subsequent experiments.

2.3 Synthesis of GelMA-g-PNIPAM Polymer

Thermoresponsive GelMA-g-PNIPAM copolymer was fabricated through a two-step methacrylation and free-radical graft polymerization strategy. Briefly, gelatin (22.5 g) was completely dissolved in 277.5 mL of phosphate-buffered saline (PBS) at 50 °C, followed by the slow addition of 11.25 mL of methacrylic anhydride (MA). After reacting for 2 h, the mixture was dialyzed against deionized water at 40 °C for 48 h with regular water replacement, frozen at −80 °C overnight, and lyophilized to obtain GelMA. Subsequently, GelMA and NIPAM were dissolved in deionized water at concentrations of 0.15 g/mL and 0.075 g/mL. After nitrogen purging for 20 min, ammonium persulfate (APS, 0.9 *wt.*% of the total monomer content) was added as the initiator, and the reaction was allowed to proceed under continuous stirring (150 rpm) at 50 °C for 8 h. During this process, PNIPAM side chains were grafted onto the GelMA backbone through APS-initiated free-radical polymerization, resulting in the

thermoresponsive polymer GelMA-g-PNIPAM. After the reaction, the gel-like product was cut into small pieces and washed thoroughly with deionized water with regular water replacement to remove unreacted NIPAM, APS, and other water-soluble impurities. The product was then transferred to a dialysis bag and dialyzed against deionized water for 7 days with regular replacement of the dialysis water to remove residual small-molecule components.

2.4 Fabrication of TA@PB-Containing GelMA-g-PNIPAM Hydrogels

Drug-loaded hydrogels were prepared using a freeze–thaw strategy. 5 mL of the prepared GelMA-g-PNIPAM precursor solution was mixed with 0.5 mL of deionized water under gentle stirring to obtain a homogeneous mixture. For the TA@PB-containing composite hydrogel, 0.5 mL of TA@PB dispersion (1 mg/mL) was used instead of deionized water. The mixtures were frozen at −20 °C for 24 h and thawed at room temperature for 8 h, with three consecutive freeze–thaw cycles, to obtain the corresponding hydrogels. For drug loading, 5 g of the preformed hydrogel was immersed in 10 mL of an aqueous solution containing 1 mg of AMX and incubated for 24 h. After loading, the residual AMX concentration in the solution was determined by UV–Vis spectroscopy at 273 nm, and the apparent loading amount was calculated from the difference between the initial and residual AMX amounts. The resulting hydrogels were denoted as GelMA-g-PNIPAM and TA@PB@GelMA-g-PNIPAM, respectively.

2.5 Characterization

Fourier transform infrared spectroscopy (FTIR, Nicolet iS10, Thermo Fisher Scientific, USA) and UV–Vis spectrophotometry (UV-4802, UNICO, China) were employed to analyze the chemical structures and optical properties of the samples. The micro/nanostructural morphology and elemental distribution were investigated using scanning electron microscopy (SEM, Apreo S, Thermo Fisher Scientific, USA) coupled with energy-dispersive X-ray spectroscopy (EDS, Aztec X-Max, Oxford Instruments, UK) for elemental mapping. The morphology structure of the nanoparticles were further characterized using transmission electron microscopy (TEM, JEM-F200, JEOL, Japan). The particle size distribution and colloidal stability of nanoparticles were determined using a dynamic light scattering and zeta potential analyzer (Zetasizer Nano ZSP, Malvern Panalytical, UK). The specific surface area, pore size distribution, and pore structural parameters of the materials were analyzed using a surface area and

porosity analyzer (ASAP 2460, Micromeritics Instrument Corporation, USA) and a mercury intrusion porosimeter (MIP, AutoPore V 9620, Micromeritics, USA). A highly sensitive differential scanning calorimeter (VP-DSC, NETZSCH, Germany) was used to investigate the thermoresponsive behavior of the hydrogels. The photothermal conversion performance was evaluated by monitoring temperature changes under 808 nm laser irradiation using an infrared thermal imaging system (TIS60+, Fluke, USA) and a thermocouple thermometer (F-8855K, FLANK, China).

2.6 Photothermal Conversion Effect

The photothermal conversion efficiency (η) of PB and TA@PB nanoparticles was determined according to a reported method based on the heating and cooling curves[46,47]. Briefly, 1 mL of nanoparticle dispersion (50 μg/mL) was irradiated with an 808 nm laser at a power density of 1.0 W/cm² with a laser spot area of 1 cm². The A808 values of PB and TA@PB dispersions were measured using UV–vis spectroscopy (Table S1). After laser irradiation, the cooling curves were recorded and fitted by plotting −ln(θ) against cooling time to obtain the time constant (τs) . The photothermal conversion efficiency was calculated using the following equation:

$$\eta = \frac{hS(T_{\max} - T_{surr}) - Q_{dis}}{I(1 - 10^{-A_{808}})} \quad (1)$$

(*hS*) is the Heat transfer coefficient, T_{max} and T_{surr} are the maximum temperature under laser irradiation and the ambient temperature, respectively. Q_{dis} is the background heat generated by the dispersion medium and container, (I) is the incident laser power, (A_{808}) is the absorbance at 808 nm. (hS) was obtained from the following equation:

$$hS = \frac{m_D C_D}{\tau_S} \quad (2)$$

(m_D) is the mass of the dispersion, (C_D) is its specific heat capacity, (τ_S) is the time constant derived from the cooling curve.

2.7 ^{1}H NMR Characterization

^{1}H NMR spectra were recorded on a 400 MHz nuclear magnetic resonance spectrometer using deuterated dimethyl sulfoxide (DMSO-d_6) as the solvent. The measurements were performed with a proton nucleus frequency of 399.87 MHz, a spectral width of approximately 20.04 ppm, an acquisition size (TD) of 64100 points, and 8 scans (NS). The chemical shifts were calibrated using the residual proton signal of DMSO-d_6 at δ = 2.50 ppm. The raw spectra were processed using MestReNova software, including phase correction, baseline correction, chemical shift calibration,

and peak identification. The characteristic proton signals of GelMA and PNIPAM segments were analyzed for structural comparison.

2.8 PBS Immersion Stability Test

The aqueous stability of the hydrogels was evaluated by measuring dry mass retention during PBS immersion[48]. The lyophilized hydrogels were weighed to determine their initial dry mass (m_0) and then immersed in 50 mL of PBS (pH 7.4) at 37 °C. At predetermined time points (1, 3, and 7 days), the samples were collected, rinsed with deionized water to remove residual salts, and lyophilized to constant weight. The final dry mass (m_t) was recorded, and the dry mass retention was calculated as follows:

$$Mass\ retention\ (\%) = \frac{m_t}{m_0} \times 100\% \quad (3)$$

2.9 Swelling Behavior of Hydrogels

The swelling properties of the hydrogels were tested using the gravimetric method[49]. Cylindrical xerogel samples (1 cm in diameter and 1 cm in thickness) of known weight (w_0) were immersed in 250 mL of PBS (pH 7.4, 0.1 M) at 25, 37, and 40 °C. At predetermined time intervals (t), the samples were removed, gently blotted to remove excess surface water, weighed (w_t), and returned to the swelling medium at the corresponding temperature until a constant weight was reached. The swelling percentage ($S\%$) at time t was calculated using the following equation:

$$S = \frac{\omega_t - \omega_0}{\omega_0} \times 100\% \quad (4)$$

2.10 Quantification of AMX Loading Efficiency

The loading efficiency of AMX was determined by an indirect quantification method[50]. Drug loading was performed by immersing 5 g of hydrogel in 10 mL of an aqueous solution containing 1 mg of AMX. The hydrogel was incubated in the drug solution for 24 h to allow drug uptake. After loading, the residual AMX concentration in the solution was determined using UV–Vis spectroscopy at 273 nm, and the amount of AMX loaded into the hydrogel was calculated from the difference between the initial and residual drug amounts. The loading efficiency was calculated according to the following equation:

$$loading\ efficience = \left(1 - \frac{M_r}{M_i}\right) \times 100\% \quad (5)$$

where M_i is the mol amount of the chemical initially in the solution and M_r is the remaining mol amount of chemical.

2.11 Stability of AMX under Incubation and NIR Irradiation Conditions

The stability of AMX under incubation and NIR irradiation conditions was evaluated. AMX solution (1 mg/mL) was prepared in PBS (pH 7.4) and incubated at 25, 37, and 40 °C for 7 days. In addition, AMX solution was irradiated with an 808 nm laser (1.0 W/cm^2) to simulate the photothermal stimulation condition. At predetermined time points, 100 μL aliquots were collected, and the AMX concentration was determined by UV–vis spectrophotometry at 273 nm. The AMX retention was calculated according to the following equation:

$$AMX\ retention = \frac{\text{AMX concentration after treatment}}{\text{Initial AMX concentration}} \times 100\% \quad (6)$$

2.12 Controlled Release of AMX

The drug-release experiments were performed in phosphate-buffered saline (PBS, pH 7.4). A 5 g sample of AMX-loaded hydrogel was immersed in 250 mL of PBS maintained at 25, 37, or 40 °C in an incubator with continuous orbital stirring at 80 rpm. At predetermined time intervals, 100 μL aliquots were withdrawn, and the AMX concentration was determined by UV–Vis spectroscopy at 273 nm using the calibration curve shown in Figure S1.

The selected volume of release medium was considered sufficient to maintain sink conditions. Assuming complete release of the initially loaded AMX, the theoretical maximum concentrations in 250 mL of PBS were estimated to be 3.73 μg/mL for GelMA-g-PNIPAM and 3.74 μg/mL for TA@PB@GelMA-g-PNIPAM, both substantially below the reported solubility of AMX in phosphate buffer.

2.13 Mechanism and Mathematical Modeling of AMX Release

The drug release data were fitted to the Korsmeyer–Peppas model to investigate the release mechanism[51]:

$$\frac{M_t}{M_\infty} = kt^n \quad (7)$$

Here, M_t and M_∞ represent the cumulative amount of AMX released at time (t) and at equilibrium, respectively. (k) is the release rate constant, and (n) is the diffusion exponent. Considering the temperature-dependent volume transition of the hydrogel,

the Korsmeyer–Peppas model was applied to the initial release stage ($M_t/M_\infty < 60\%$) as an empirical description of the release behavior.

2.14 Photothermal Performance of the Hydrogel

A cubic TA@PB@GelMA-g-PNIPAM hydrogel specimen (1 cm × 1 cm × 1 cm, approximately 1 cm^3) was irradiated with an 808 nm NIR laser at a power density of 1.0 W/cm^2 for 6 min. The initial temperature was set to 25 °C. The hydrogel surface temperature was recorded at regular intervals using the temperature-measurement device described in Section 2.5. A blank GelMA-g-PNIPAM hydrogel of the same dimensions was evaluated under identical conditions as a control. The recorded temperature values represent the surface temperature.

2.15 In *Vitro* Cell Tests

Cytocompatibility was evaluated using the CCK-8 assay and live/dead staining. Hydrogel samples (50 mg) were immersed in 1mL of complete DMEM and incubated at 37 °C for 24 h, after which the supernatants were collected as hydrogel extracts. Complete DMEM was used for the control group. NIH3T3 cells were seeded into 96-well plates at a density of 5×10^3 cells per well and cultured with complete DMEM or hydrogel extracts for 24 or 48 h, followed by the addition of CCK-8 solution according to the manufacturer's instructions. The absorbance was measured at 450 nm using a microplate reader, with cell-free medium and extract blank wells included for background correction, and cell viability was normalized to that of the control group. CCK-8 assay were performed in triplicate (n = 3). Cell viability was calculated according to the following equation[52]:

$$Cell\ viability = \frac{OD_{sample} - OD_{blank}}{OD_{control} - OD_{blank}} \times 100\% \quad (8)$$

For live/dead staining, NIH3T3 cells were seeded into 24-well plates at a density of 2×10^4 cells per well and cultured with complete DMEM or hydrogel extracts for 48 h, followed by staining with Calcein-AM/PI working solution according to the manufacturer's instructions. The stained cells were observed and imaged using a fluorescence microscope, with live and dead cells identified by green and red fluorescence, respectively.

3. Results and Discussion

3.1 Construction and Interfacial Characterization of TA-Modified PB Nanoparticles

PB nanoparticles were selected as photothermal components because of their intrinsic near-infrared absorption and efficient photothermal conversion capability. To improve the dispersion stability and interfacial compatibility of PB nanoparticles within the polymer network, TA was introduced onto the PB surface through surface modification, generating TA@PB. TEM was first employed to examine the morphology of pristine PB and TA@PB. As shown in Figure 1a, pristine PB exhibited a typical cubic morphology with an average particle size of approximately 50 nm, indicating successful formation of uniform PB nanocrystals. After TA modification, an altered surface contrast was observed around the PB nanoparticles (Figure 1b), indicating the successful deposition of TA without affecting the PB structure. The dispersion behavior of PB and TA@PB nanoparticles was further investigated. As shown in Figure 1c, TA@PB dispersions exhibited the characteristic dark-blue color of PB. Dynamic light scattering (DLS) analysis showed that TA modification slightly increased the hydrodynamic diameter of PB nanoparticles, which was attributed to the formation of a TA-derived surface layer (Figure 1d, e). The particle size remained within the nanoscale range after modification, indicating that the TA coating process did not induce significant aggregation. The surface charge variation after TA modification was evaluated by zeta potential measurement. As shown in Figure 1f, pristine PB exhibited a negative surface potential of approximately −38 mV, whereas TA@PB showed a more negative value of approximately −50 mV. The increased negative charge was associated with the phenolic hydroxyl groups introduced by TA, confirming the successful modification of the PB surface.

UV–Vis absorption spectroscopy further confirmed the successful fabrication of TA@PB nanoparticles. As shown in Figure 1g, both PB and TA@PB exhibited the characteristic absorption band near 690 nm associated with intervalence charge transfer between Fe^{2+} and Fe^{3+} centers, confirming that the PB electronic structure was preserved after modification. In addition, TA@PB displayed an additional absorption feature around 275 nm, corresponding to the aromatic phenolic structure of TA, providing direct evidence for the successful introduction of TA onto the PB surface. FTIR spectra further revealed the interaction between TA and PB (Figure 1h). Pristine PB exhibited the characteristic C≡N stretching vibration near 2080 cm^{-1} and Fe–CN–Fe vibration bands in the low-wavenumber region, confirming the formation of the PB

coordination framework. After TA modification, the O–H stretching vibration associated with phenolic groups was altered, accompanied by changes in the C≡N vibration region, indicating interactions between TA hydroxyl groups and surface iron sites through coordination and hydrogen-bonding interactions.

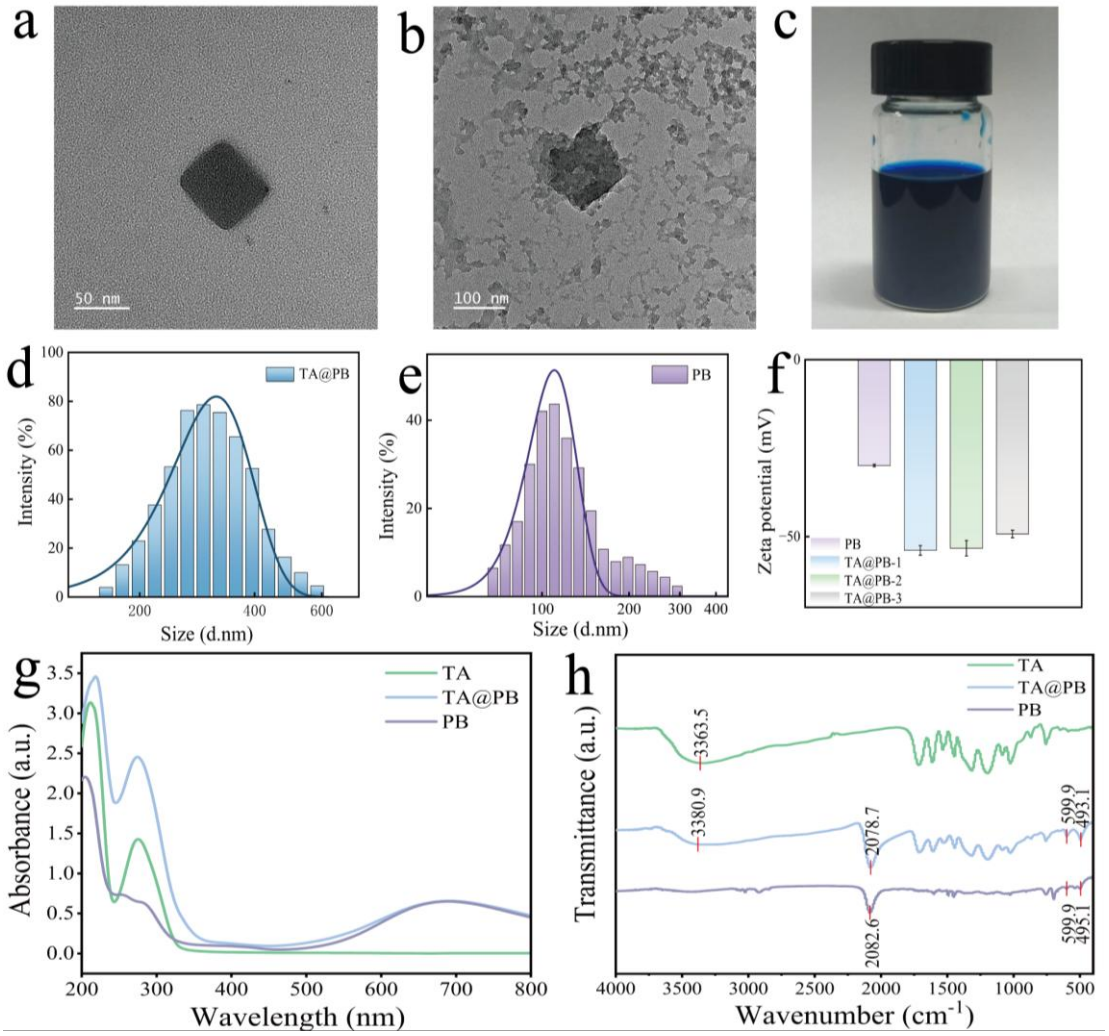

Figure 1. Characterizations of TA@PB nanoparticles. TEM images of (a) PB and (b) TA@PB nanoparticles. Scale bar = 50 nm and 100 nm, respectively. (c) Photograph of the TA@PB solution. Size distribution histograms of (d) TA@PB and (e) PB. (f) Zeta potential of TA@PB and PB nanoparticles (TA@PB-1, TA@PB-2, and TA@PB-3, with TA/PB volume ratios of 2:1, 1:1, and 1:2, respectively). (g) UV-Vis-NIR spectra and (h) FTIR spectra of the prepared TA, PB, and TA@PB.

3.2 Photothermal Conversion and Thermal Regulation Capability of TA@PB Nanoparticles

The photothermal conversion behavior of TA@PB nanoparticles was investigated to evaluate the effect of TA modification on the light-to-heat conversion capability of PB

nanoparticles. The proposed photothermal conversion process of TA@PB nanoparticles is illustrated in Figure 2a. Upon 808 nm laser irradiation, PB nanoparticles absorb NIR light through the electronic transition associated with the Fe^{2+}/Fe^{3+} mixed-valence structure, followed by nonradiative relaxation and conversion of absorbed energy into thermal energy. To investigate the influence of TA modification on the photothermal performance of PB nanoparticles, TA@PB nanoparticles with different TA contents were prepared and subjected to 808 nm laser irradiation. As shown in Figure 2b, the photothermal response increased gradually with increasing TA content. The samples containing higher TA concentrations exhibited a faster temperature increase and reached higher equilibrium temperatures under identical irradiation conditions. This result indicates that TA modification contributes to the enhanced photothermal heating behavior of PB nanoparticles. The photothermal heating and cooling behaviors of PB and TA@PB nanoparticles were further compared under 808 nm laser irradiation. As shown in Figure 2c, both PB and TA@PB exhibited rapid temperature increases during laser irradiation, followed by gradual temperature decreases after removal of the laser source. Compared with pristine PB, TA@PB showed a higher temperature elevation under identical irradiation conditions. Based on the photothermal heating–cooling curves, the photothermal conversion efficiency was calculated according to the reported method. TA@PB exhibited an enhanced photothermal conversion efficiency of approximately 50.9%, compared with 30.7% for pristine PB, indicating that TA modification promoted the conversion of absorbed NIR energy into heat. The photothermal stability of PB and TA@PB nanoparticles was evaluated by repeated irradiation cycles. As shown in Figure 2d, pristine PB maintained a relatively stable heating response over four consecutive irradiation cycles. Similarly, TA@PB exhibited reproducible temperature elevation profiles during repeated irradiation (Figure 2e), with no obvious decrease in photothermal performance. These results indicate that TA modification does not compromise the photothermal stability of PB nanoparticles. To examine the structural stability of TA@PB nanoparticles after photothermal treatment, TEM characterization was performed after laser irradiation. As shown in Figure 2f, TA@PB nanoparticles retained their original morphology without apparent aggregation or structural damage after irradiation, confirming their stability under repeated photothermal activation. The spatial temperature distribution generated by PB and TA@PB nanoparticles was further analyzed using infrared thermal imaging. As shown in Figure 2g, both PB and TA@PB dispersions exhibited gradual temperature increases

during 150 s of 808 nm laser irradiation. Compared with PB, TA@PB produced a higher thermal signal over the irradiated region, consistent with the enhanced temperature elevation observed in the photothermal heating curves. These results demonstrate that TA modification improves the photothermal heating performance of PB nanoparticles while maintaining their structural stability during repeated irradiation. The TA@PB nanoparticles therefore exhibit stable NIR-triggered photothermal conversion characteristics.

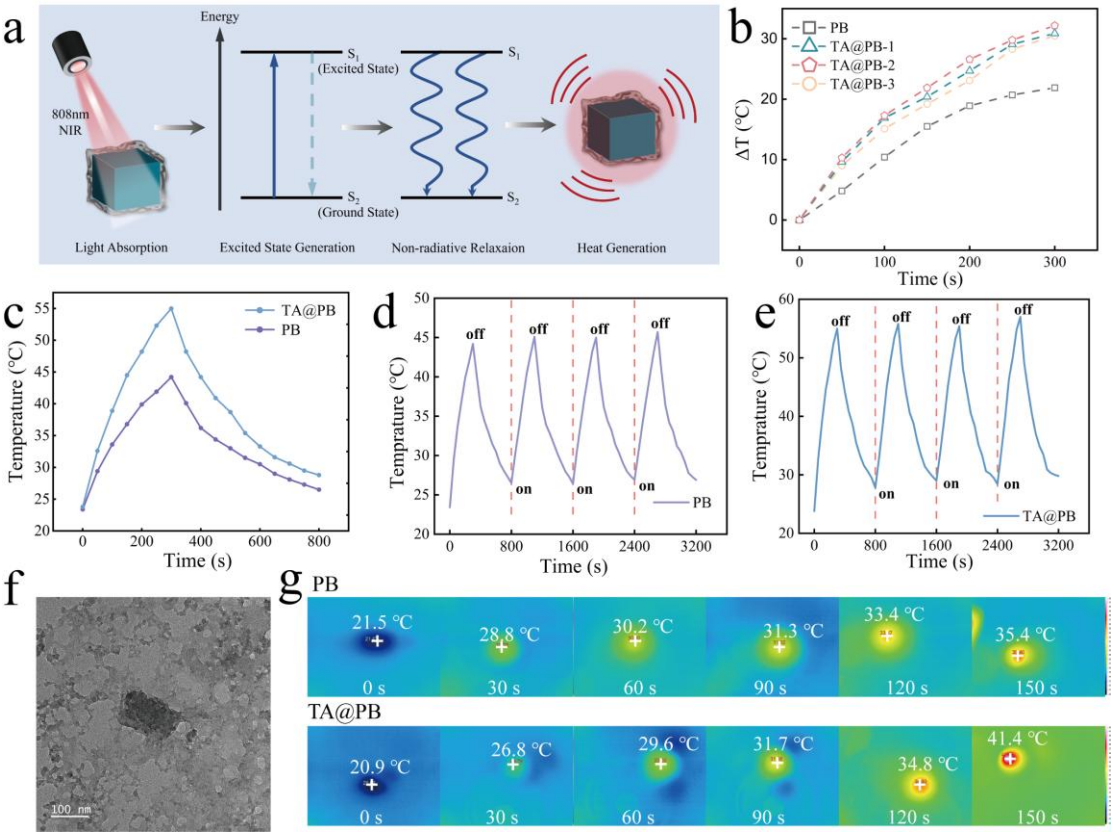

Figure 2. Photothermal properties of TA@PB nanoparticles. (a) Schematic illustration of the photothermal conversion mechanism of TA@PB nanoparticles. (b) Temperature change (ΔT) profiles of PB and TA@PB with different TA contents (TA@PB-1, TA@PB-2, and TA@PB-3, with TA/PB volume ratios of 2:1, 1:1, and 1:2, respectively) under 808 nm irradiation (1.0 W/cm^2) for 5 min. (c) Heating and cooling curves of PB and TA@PB under 808 nm. Photothermal profiles of (d) PB and (e) TA@PB over 4 cycles under 808 nm irradiation (1.5 W/cm^2). (f) TEM image of TA@PB after laser irradiation. (g) Thermal distribution maps of PB and TA@PB over 150 s under 808 nm laser irradiation (1.0 W/cm^2).

3.3 Construction of GelMA-g-PNIPAM Polymer and Thermoresponsive Behavior

The GelMA-g-PNIPAM polymer network was constructed through sequential methacrylation of gelatin and free-radical graft polymerization of NIPAM. The synthetic strategy is illustrated in Figure 3a. Methacryloyl groups were first introduced onto the gelatin backbone to provide polymerizable sites, followed by graft polymerization of NIPAM to generate PNIPAM side chains. This design produced a polymer architecture in which gelatin served as the backbone and PNIPAM acted as the thermoresponsive segment. The degree of methacrylation of gelatin was first evaluated by ninhydrin assay. As shown in Figure 3b, pristine gelatin exhibited a strong absorbance at 565 nm due to the reaction between free amino groups and ninhydrin. After methacrylation, the absorbance intensity decreased markedly, indicating the consumption of amino groups during reaction with methacrylic anhydride. Quantitative analysis based on the glycine calibration curve (Figure S2) showed that the free amino group content decreased from 9.37 mg/mL for gelatin to 0.42 mg/mL for GelMA, corresponding to a methacrylation degree of approximately 95%. These results confirm the successful introduction of methacryloyl groups onto gelatin molecules. The chemical structure evolution during polymer modification was further investigated by FTIR spectroscopy (Figure 3c). Gelatin exhibited characteristic absorption bands at approximately 3300 cm^{-1} (O–H and N–H stretching), 1650 cm^{-1} (amide I), and 1540 cm^{-1} (amide II), corresponding to the protein backbone structure. After methacrylation, the characteristic gelatin peaks were retained, while new absorption features associated with methacryloyl groups appeared, confirming the successful modification of gelatin. Following NIPAM graft polymerization, additional characteristic peaks corresponding to PNIPAM segments were observed, including the C–H stretching vibration of isopropyl groups and amide-related vibrations. These spectral changes support the incorporation of PNIPAM into the GelMA-derived polymer; this assignment was further examined by ^{1}H NMR.. The incorporation of TA@PB nanoparticles into the GelMA-g-PNIPAM network was further verified by FTIR analysis. Compared with GelMA-g-PNIPAM, the TA@PB-containing sample exhibited additional absorption features associated with polyphenolic TA components and PB coordination structures. The retention of characteristic polymer absorption bands indicates that nanoparticle incorporation did not disrupt the chemical structure of the polymer network.

To further distinguish the chemical grafting of PNIPAM onto GelMA from their physical blending, ^{1}H NMR spectroscopy was employed to investigate the structural evolution of the polymer (Figure S3). The methyl proton signal of the isopropyl group

in PNIPAM can serve as a characteristic indicator of PNIPAM chain incorporation, while the variation of the methacryloyl vinyl proton signals in GelMA reflects the consumption of reactive sites during polymerization; therefore, these two signals were selected for structural verification. GelMA exhibited characteristic signals corresponding to the methacryloyl vinyl protons at approximately 5.24 and 5.56 ppm, whereas PNIPAM showed a characteristic peak at around 1.05 ppm attributed to the methyl protons of the isopropyl group. The GelMA/PNIPAM physical mixture retained both characteristic signals, indicating the coexistence of the two components through physical blending. After graft polymerization and purification, the GelMA-g-PNIPAM sample maintained the characteristic PNIPAM signal at approximately 1.05 ppm, while the vinyl proton signals were significantly reduced, suggesting the consumption of methacryloyl groups during the free-radical polymerization process. Combined with the FTIR results of the purified product, these findings further support the successful incorporation of PNIPAM chains into the GelMA-derived polymer network. The macroscopic appearance of GelMA-g-PNIPAM and TA@PB@GelMA-g-PNIPAM hydrogels is shown in Figure S4. GelMA-g-PNIPAM exhibited a transparent appearance, whereas TA@PB@GelMA-g-PNIPAM showed a uniform blue color due to the characteristic color of PB.

The thermal transition behavior of GelMA-g-PNIPAM networks was investigated by DSC (Figure 3d). Both GelMA-g-PNIPAM and TA@PB@GelMA-g-PNIPAM networks exhibited endothermic transitions near the LCST region of PNIPAM. The transition temperature was measured as approximately 31 °C for both GelMA-g-PNIPAM and TA@PB@GelMA-g-PNIPAM, indicating that incorporation of TA@PB had limited influence on the intrinsic thermal transition of PNIPAM chains. The comparable LCST values demonstrate that PNIPAM segments maintained their reversible hydration–dehydration behavior after grafting onto the gelatin backbone and incorporation of nanoparticles. The temperature-dependent morphology transition was further examined by visual observation (Figure 3e). At temperatures below the LCST, the hydrogel maintained a swollen and transparent state due to the hydrated conformation of PNIPAM chains. Upon increasing temperature above the transition point, the hydrogel gradually became opaque and contracted, corresponding to the dehydration and aggregation of PNIPAM segments. The reversible transition upon temperature variation confirms that the grafted PNIPAM chains retained their thermoresponsive characteristics within the GelMA-based polymer network.

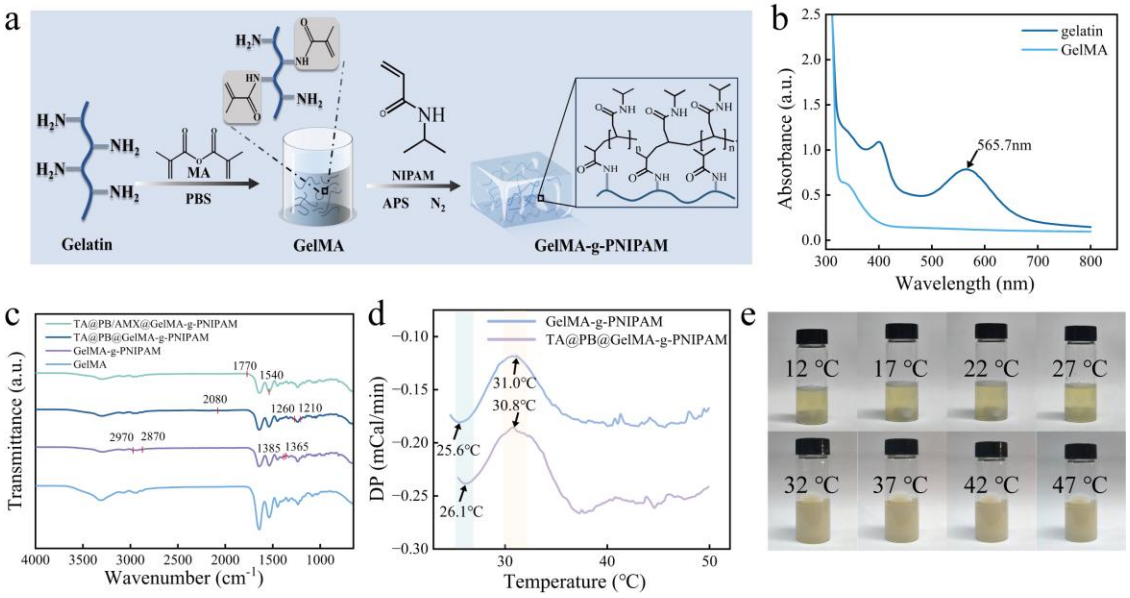

Figure 3. (a) Schematic illustration of the synthesis process of GelMA-g-PNIPAM polymer networks. (b) Ninhydrin analysis of gelatin before and after methacrylation. (c) FTIR spectra of gelatin, GelMA, GelMA-g-PNIPAM, TA@PB/AMX@GelMA-g-PNIPAM, and TA@PB@GelMA-g-PNIPAM networks. (d) DSC curves of GelMA-g-PNIPAM and TA@PB@GelMA-g-PNIPAM polymers. (e) Temperature-dependent morphology changes of GelMA-g-PNIPAM polymers.

3.4 TA@PB and PNIPAM-Mediated Modulation of Hierarchical Network Structure in GelMA-g-PNIPAM Hydrogels

To investigate the influence of PNIPAM graft chains and TA@PB nanoparticles on the hierarchical structure of GelMA-based hydrogels, mercury intrusion porosimetry (MIP) and microscopic characterization were performed. The structural differences between GelMA and TA@PB@GelMA-g-PNIPAM hydrogels were systematically analyzed. The macroporous characteristics of the lyophilized hydrogels were first evaluated by MIP. As shown in Figure 4a, both hydrogels exhibited continuously increasing cumulative mercury intrusion volumes with increasing pressure, indicating the formation of mercury-accessible porous structures. Quantitative analysis of the MIP parameters (Table S2) revealed that the total pore volume increased from 2.5871 mL/g for GelMA to 14.7337 mL/g for TA@PB@GelMA-g-PNIPAM. Meanwhile, the porosity increased from 75.2249% to 91.2750%, accompanied by a decrease in bulk density from 0.2908 g/mL to 0.0619 g/mL. These results indicate that the introduction of PNIPAM segments and TA@PB nanoparticles altered the network formation process and generated a hydrogel structure with higher porosity and pore volume in the dry

state. The pore size distribution obtained from MIP analysis is shown in Figure 4b, c. Both hydrogels exhibited broad pore distributions, indicating the presence of multiscale porous structures. Compared with GelMA, GelMA-g-PNIPAM and TA@PB@GelMA-g-PNIPAM exhibited comparable pore characteristics, with a higher pore volume contribution in the main pore size region than GelMA and only minor differences between the two composites (Table S2). These results suggest that PNIPAM incorporation increased pore development in the dried samples, whereas TA@PB had little effect on overall porosity. Notably, the comparable average pore sizes between the two samples indicate that the increased porosity mainly originated from the increased pore volume and improved pore connectivity rather than simple enlargement of individual pores. BET analysis provided complementary information on the surface area and pore characteristics of the hydrogels. TA@PB@GelMA-g-PNIPAM exhibited a higher specific surface area than GelMA, suggesting changes in the accessible surface structure following network modification (Figures S5–7).

The morphology of the freeze-dried hydrogel networks was examined by SEM. As shown in Figure 4d, the GelMA hydrogel exhibited an irregular porous structure with relatively discontinuous pore channels. In contrast, TA@PB@GelMA-g-PNIPAM displayed a more interconnected porous morphology with improved pore wall continuity (Figure 4e, f). The SEM observations were consistent with the MIP and BET results, confirming the structural differences generated after incorporation of PNIPAM segments and TA@PB nanoparticles. The distribution of TA@PB nanoparticles within the hydrogel matrix was further examined by EDS elemental mapping. As shown in Figure 4g, C, N, and O elements derived from the polymer matrix were uniformly distributed throughout the hydrogel, while Fe signals originating from PB nanoparticles were evenly dispersed without obvious aggregation. These results confirm the successful incorporation and homogeneous distribution of TA@PB within the GelMA-g-PNIPAM network. Regarding the network stabilization mechanism, PNIPAM chains are covalently grafted onto the GelMA backbone, while network stability may also be influenced by physical associations. At 37 and 40 °C, PNIPAM segments undergo dehydration and enhanced hydrophobic association, which may work together with chain entanglement and interchain hydrogen bonding to maintain network cohesion. The PBS immersion stability test (Figure S8) showed that the hydrogels retained 98.95%–99.24% of their initial dry mass after 7 days of immersion, indicating good stability under the tested conditions.

Based on the above structural analyses, a possible formation mechanism of the hierarchical porous network is proposed in Figure 4h. During freeze-thaw treatment, PNIPAM graft chains participate in the rearrangement of the polymer network, while TA@PB nanoparticles provide additional interfaces that may influence polymer chain organization. The combined effects of polymer chain reorganization and nanoparticle incorporation affect ice crystal formation and the subsequent pore generation process.

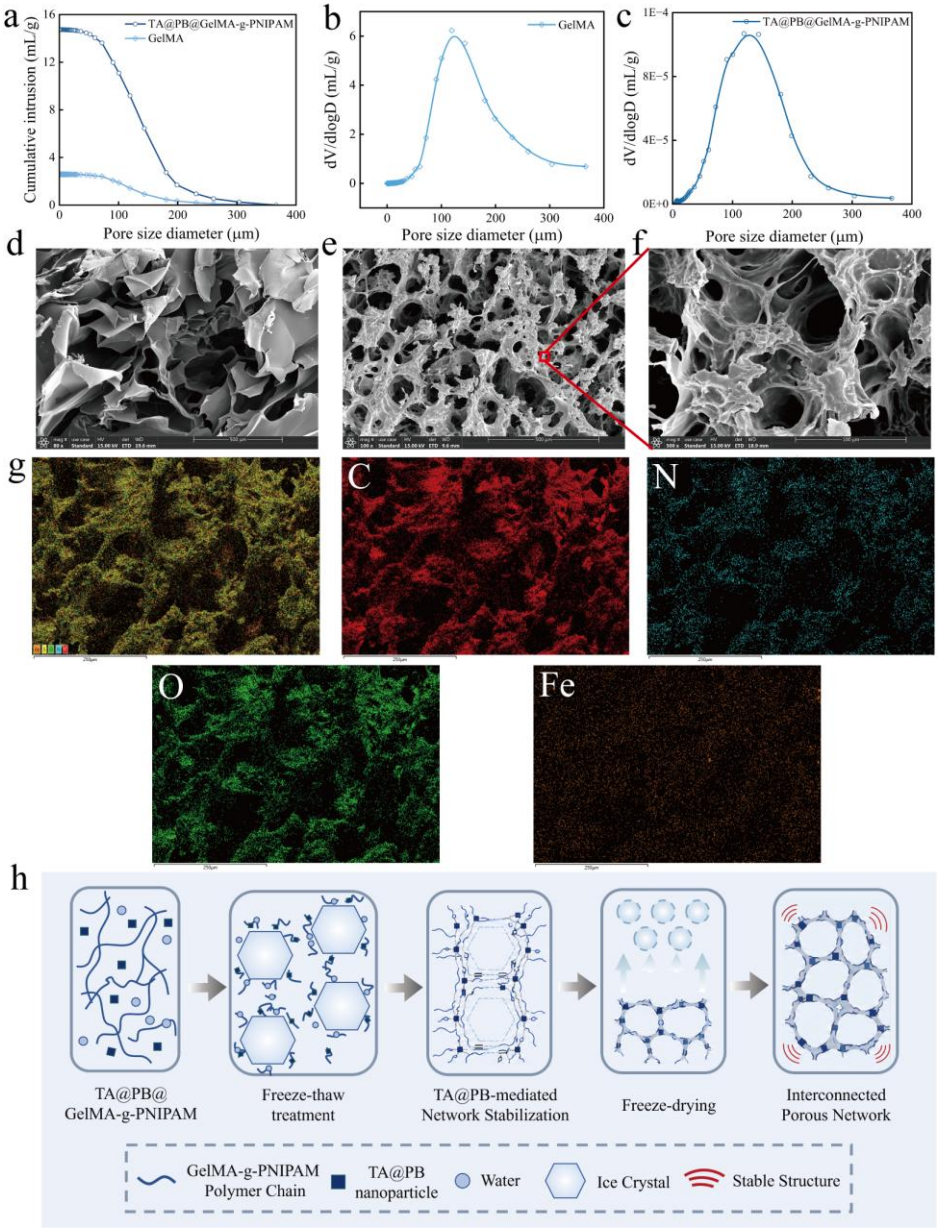

Figure 4. Multiscale pore structure and formation mechanism characterization of hydrogels. Mercury intrusion porosimetry analysis of GelMA and TA@PB@GelMA-g-PNIPAM hydrogels, including cumulative intrusion curves (a) and pore size distribution curves (b, c). SEM images of GelMA hydrogel (d) and TA@PB@GelMA-g-PNIPAM hydrogel (e, f) at different magnifications. (g) EDS elemental mapping

analysis of C, N, O, and Fe elements in TA@PB@GelMA-g-PNIPAM hydrogel. (h) Schematic illustration of the formation of hierarchical porous network structure.

3.5 Photothermal-Regulated Drug Release of TA@PB@GelMA-g-PNIPAM Hydrogels

The temperature-responsive swelling behavior and drug release characteristics of TA@PB@GelMA-g-PNIPAM hydrogels were investigated to evaluate the influence of PNIPAM chain transition and photothermal stimulation on drug delivery behavior. The swelling behavior of the hydrogels was first evaluated at different temperatures. As shown in Figure 5a–c, all hydrogels exhibited rapid water absorption during the initial stage, followed by gradual stabilization with prolonged immersion time. The equilibrium swelling ratios were temperature-dependent, with the highest swelling capacity observed at 25 °C. Compared with GelMA-g-PNIPAM, TA@PB-containing hydrogels exhibited slightly increased swelling ratios at 25, 37, and 40 °C, which may be associated with the increased hydrophilicity and structural changes introduced by TA@PB incorporation. With increasing temperature, the swelling ratio decreased gradually due to the reversible hydration transition of PNIPAM segments. At temperatures below the LCST, PNIPAM chains remain hydrated through hydrogen bonding with water molecules, whereas elevated temperatures induce dehydration and chain contraction, resulting in reduced water uptake. The influence of temperature-dependent network transition on drug release (AMX) was subsequently investigated. UV–Vis calibration curve of AMX at 273 nm and the corresponding linear regression are shown in Figure S9. The loading efficiency was 93.23 ± 0.55% (0.9323 ± 0.0055 mg) for GelMA-g-PNIPAM and 93.40 ± 0.66% (0.9340 ± 0.0066 mg) for TA@PB@GelMA-g-PNIPAM, with three independent measurements for each group, calculated as the mass ratio of AMX retained in the hydrogel to the drug mass initially placed in contact with the hydrogel after 24 h (Table S3). To exclude the possibility that AMX degradation contributed to the observed release behavior, the stability of AMX under different incubation conditions was evaluated. As shown in Figure S10, AMX retained more than 97% of its initial concentration after incubation at 25, 37, and 40 °C for 7 days, indicating negligible AMX loss under the experimental conditions. As shown in Figure 5d, the cumulative drug release profiles exhibited clear temperature dependence. The hydrogel showed slower release at 25 °C, while the release rate increased at 37 and 40 °C. After 3 days, the cumulative release reached approximately

42.57% at 25 °C, 81.24% at 37 °C, and 92.61% at 40 °C, respectively. The accelerated release at elevated temperatures was attributed to the dehydration and conformational transition of PNIPAM segments, which altered the hydration state and diffusion environment of the polymer network, facilitating drug diffusion.

To further analyze the drug release mechanism, different kinetic models were applied to fit the release profiles. At 37 °C, the Korsmeyer–Peppas model exhibited the highest fitting correlation coefficient (R^2 = 0.99089), which was higher than those of the Higuchi model (R^2 = 0.94621), first-order model (R^2 = 0.89052), and zero-order model (R^2 = 0.80210) (Table S4). These results indicated that the Korsmeyer–Peppas model provided a better description of the drug release behavior. The temperature-dependent release kinetics were further evaluated using the Korsmeyer–Peppas model at 25, 37, and 40 °C (Figure 5e and Table S5). Given the temperature-dependent volume transition of the hydrogel, the model was used as an empirical description of the initial release stage ($M_t/M\infty < 60\%$). The fitting results showed high correlation coefficients of 0.97923, 0.99089, and 0.98927, respectively. Meanwhile, the release rate constant (k) increased from 0.11 at 25 °C to 0.19 at 37 °C and 0.23 at 40 °C, indicating accelerated drug release with increasing temperature. The calculated diffusion exponents (n) were 0.26, 0.32, and 0.31, respectively. For cylindrical drug delivery systems, an n value of approximately 0.45 corresponds to ideal Fickian diffusion. The obtained n values suggest a restricted diffusion process rather than ideal Fickian transport. This behavior is attributed to the thermally induced PNIPAM contraction above the LCST, which changes network hydration, drug partitioning, and diffusion pathways.

The photothermal response of the hydrogel was evaluated under 808 nm NIR irradiation, with an initial temperature of 25 °C. As shown in Figure 5f, the surface temperature of the TA@PB@GelMA-g-PNIPAM hydrogel increased progressively upon NIR irradiation, whereas the blank GelMA-g-PNIPAM hydrogel exhibited only a slight temperature change under identical conditions.The remote regulation of drug release through photothermal stimulation was further investigated using cyclic NIR irradiation. As shown in Figure 5g, with 25 °C as the baseline temperature, the release profile displayed periodic changes corresponding to the laser on and off cycles. During NIR irradiation, the release rate increased, whereas the release slowed after removing the laser irradiation. This reversible response resulted from the photothermal conversion of PB nanoparticles, generating local heating and inducing the PNIPAM

volume transition, thereby altering the diffusion environment and accelerating AMX release. When irradiation was removed, the temperature decreased and the polymer network gradually recovered its hydrated state, resulting in reduced drug diffusion. These results demonstrate that TA@PB incorporation enables externally controlled drug release through NIR-triggered photothermal regulation.

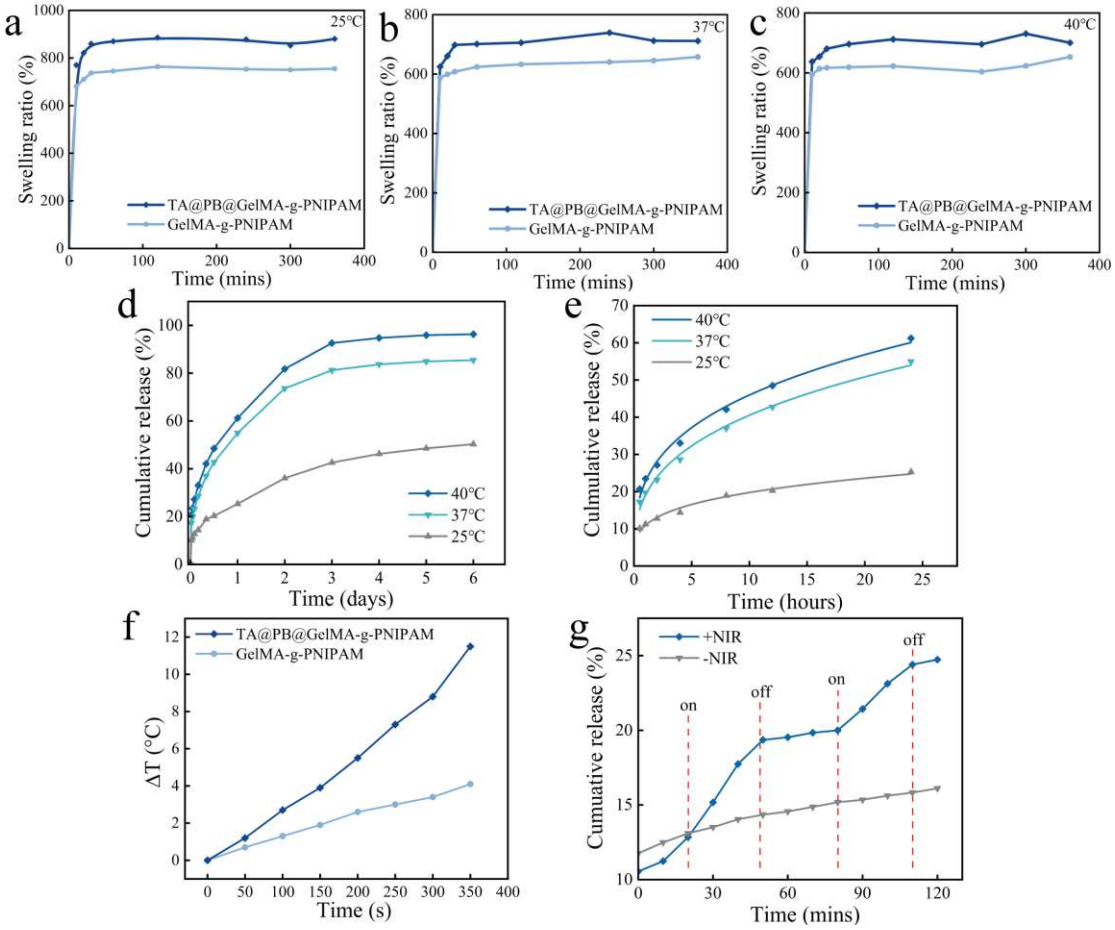

Figure 5. Stimuli-responsive swelling and controlled drug release of TA@PB@GelMA-g-PNIPAM hydrogels. Time-dependent swelling profiles of the hydrogels at 25 °C (a) ,37 °C (b), and 40 °C (c). The cumulative drug release profiles at different temperatures (d), Korsmeyer–Peppas model fitting of cumulative drug release from the TA@PB@GelMA-g-PNIPAM hydrogel at 25 °C, 37 °C, and 40 °C (e). Temperature change (ΔT) profiles of TA@PB@GelMA-g-PNIPAM and GelMA-g-PNIPAM (f). NIR-triggered drug release under cyclic laser on/off irradiation (g).

3.6 In Vitro Cytocompatibility

To evaluate the cytocompatibility of the TA@PB@GelMA-g-PNIPAM hydrogel, NIH/3T3 fibroblasts were subjected to live/dead staining and CCK-8 cell viability

assays. The cells were cultured with the control medium or hydrogel extracts and analyzed at the corresponding time points. The live/dead staining results showed that the cells in all groups were predominantly green, with intact cell morphology and no obvious increase in red fluorescence at 24 and 48 h, indicating that the TA@PB@GelMA-g-PNIPAM hydrogel did not cause apparent adverse effects on NIH/3T3 cells (Figure 6a). The CCK-8 results showed that cell viability remained at a relatively high level throughout the culture period, with the mean cell viability exceeding 85% at 48 h (Figure 6b), indicating that the hydrogel extracts exhibited no obvious cytotoxicity and that the TA@PB@GelMA-g-PNIPAM hydrogel possessed good cytocompatibility.

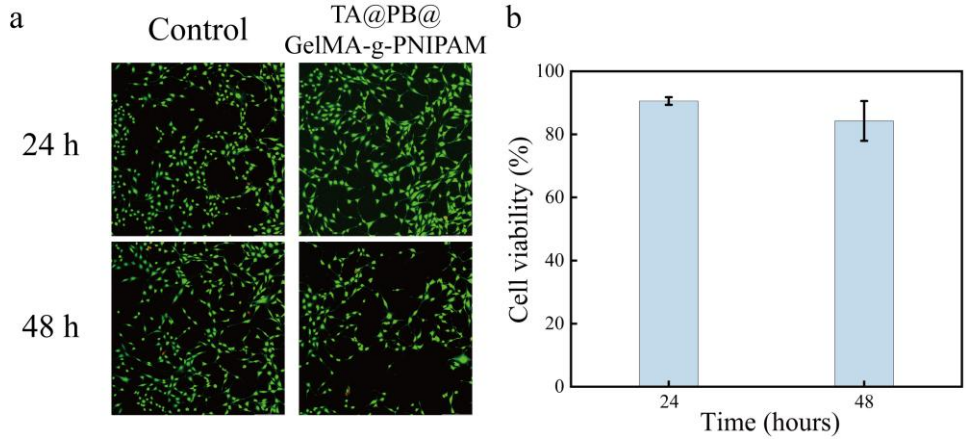

Figure 6. Cytocompatibility of the TA@PB@GelMA-g-PNIPAM hydrogel evaluated using NIH/3T3 fibroblasts. (a) Representative live/dead staining images of NIH/3T3 cells after incubation with the control medium and hydrogel extracts for 24 and 48 h. Green fluorescence indicates living cells, while red fluorescence indicates dead cells. (b) CCK-8 assay results showing the viability of NIH/3T3 cells after incubation for 24 and 48 h. Data are presented as mean ± SD, n = 3.

4. Conclusions

In this work, a photothermally regulated GelMA-g-PNIPAM hydrogel was constructed by combining a thermoresponsive polymer architecture with TA-modified Prussian blue nanoparticles. Grafting PNIPAM onto the GelMA backbone introduced a reversible thermal transition at approximately 31 °C, while TA@PB nanoparticles provided stable NIR-responsive photothermal conversion and were homogeneously incorporated within the polymer matrix. PNIPAM grafting markedly altered the porous architecture of the gelatin-based network, whereas TA@PB incorporation had only a

limited additional effect on the overall porosity. More importantly, TA@PB converted 808 nm NIR irradiation into localized thermal signals that induced the PNIPAM volume transition and thereby regulated the hydration state and drug-release behavior of the hydrogel. The cumulative AMX release increased from 42.57% at 25 °C to 92.61% at 40 °C after 3 days, and cyclic NIR irradiation produced corresponding changes in the release profile, demonstrating remote photothermal regulation of drug release. These results establish a nanoparticle–polymer coupling strategy in which an external optical stimulus is translated into a thermoresponsive polymer transition, providing a design approach for remotely regulated drug-delivery polymer networks.

CRediT authorship contribution statement

Zehua Jiao: Data curation, Investigation, Methodology, Writing – original draft. **Tong Shao:** Data curation, Formal analysis, Investigation, Methodology. **Fanying Zeng:** Formal analysis, Investigation. **Shaojian Lin:** Supervision, Project administration, Resources. **Jianwu Lan**: Supervision, Project administration, Resources. **Guolin He**: Investigation, Methodology, Writing – review & editing. **Jiaojiao Shang:** Conceptualization, Formal analysis, Methodology, Funding acquisition, Project administration, Resources, Supervision, Writing – review & editing.

Declaration of competing interest

The authors declare that they have no known competing financial interests or personal relationships that could have appeared to influence the work reported in this paper.

Acknowledgement

This work was supported by Institutional Research Fund from Sichuan University (Grant No. 2024SCUQJTX020).

Data availability

The data that support the findings of this study are available from the corresponding author upon reasonable request.

References

[1] E. Norouzi Farahani, S. Arzemanzadeh, M. Mahnama, E. Hosseinian, Atomistic insights into the mechanical properties of cross-linked Poly(N-

isopropylacrylamide) hydrogel, Polymer 297 (2024) https://doi.org/10.1016/j.polymer.2024.126798.
[2] D.J. Beebe, J.S. Moore, J.M. Bauer, Q. Yu, R.H. Liu, C. Devadoss, B.H. Jo, Functional hydrogel structures for autonomous flow control inside microfluidic channels, Nature 404 (2000) 588-590. https://doi.org/10.1038/35007047.
[3] M.A. Stuart, W.T. Huck, J. Genzer, M. Muller, C. Ober, M. Stamm, G.B. Sukhorukov, I. Szleifer, V.V. Tsukruk, M. Urban, F. Winnik, S. Zauscher, I. Luzinov, S. Minko, Emerging applications of stimuli-responsive polymer materials, Nat Mater 9 (2010) 101-113. https://doi.org/10.1038/nmat2614.
[4] Z. Wang, Y. Li, X. Wang, M. Pi, B. Yan, R. Ran, A rapidly responsive, controllable, and reversible photo-thermal dual response hydrogel, Polymer 237 (2021) https://doi.org/10.1016/j.polymer.2021.124344.
[5] J. Gao, P. Luo, S. Shen, Y. Liu, X. Li, X. Wang, Enzyme- and GSH-responsive gelatin-coated magnetic multi-shell hollow mesoporous organosilicon nanoparticles for avermectin controlled release, Collagen Leather 7 (2025) 10. https://doi.org/10.1186/s42825-025-00191-z.
[6] W. Zou, J. Dong, Y. Luo, Q. Zhao, T. Xie, Dynamic Covalent Polymer Networks: from Old Chemistry to Modern Day Innovations, Adv Mater 29 (2017) https://doi.org/10.1002/adma.201606100.
[7] E.J. Choi, S. Ha, J. Lee, T. Premkumar, C. Song, UV-mediated synthesis of pNIPAM-crosslinked double-network alginate hydrogels: Enhanced mechanical and shape-memory properties by metal ions and temperature, Polymer 149 (2018) 206-212. https://doi.org/10.1016/j.polymer.2018.06.080.
[8] Y. Qiu, K. Park, Environment-sensitive hydrogels for drug delivery, Adv Drug Deliv Rev 53 (2001) 321-339. https://doi.org/10.1016/s0169-409x(01)00203-4.
[9] Y. Qian, S. Lu, J. Meng, W. Chen, J. Li, Thermo-Responsive Hydrogels Coupled with Photothermal Agents for Biomedical Applications, Macromol Biosci 23 (2023) e2300214. https://doi.org/10.1002/mabi.202300214.
[10] A.J. Rosario, B. Ma, Stimuli-Responsive Polymer Networks: Application, Design, and Computational Exploration, ACS Applied Polymer Materials 6 (2024) 14204-14228. https://doi.org/10.1021/acsapm.4c00002.
[11] H. Zhang, Y. Wu, J. Yang, D. Wang, P. Yu, C.T. Lai, A.C. Shi, J. Wang, S. Cui, J. Xiang, N. Zhao, J. Xu, Superstretchable Dynamic Polymer Networks, Adv Mater 31 (2019) e1904029. https://doi.org/10.1002/adma.201904029.

[12] A.M. Wemyss, C. Ellingford, Y. Morishita, C. Bowen, C. Wan, Dynamic Polymer Networks: A New Avenue towards Sustainable and Advanced Soft Machines, Angew Chem Int Ed Engl 60 (2021) 13725-13736. https://doi.org/10.1002/anie.202013254.

[13] A. Jangizehi, P. Föckler, O. Pazer, M. Ahmadi, S. Seiffert, Light- and heat-responsive interpenetrating polymer networks for solar-driven water desalination, Polymer 351 (2026) https://doi.org/10.1016/j.polymer.2026.129845.

[14] X. Zheng, Y. Zhang, N. Dan, Y. Chen, Z. Li, Y. Wang, Multifunctional hydrogel–acellular dermal matrix composite patch: an anticalcification barrier with antibacterial and anti-inflammatory properties for abdominal wall repair, Collagen and Leather 7 (2025) 31. https://doi.org/10.1186/s42825-025-00211-y.

[15] Q. Liu, W. Dai, Y. Gao, S. Li, X. Zhao, H. Jia, Y. Tan, L. Guo, Y. Fan, X. Zhang, The degradation rate of collagen-based hydrogels regulates chondrogenic differentiation of bone marrow mesenchymal stem cells, Collagen Leather 7 (2025) 39. https://doi.org/10.1186/s42825-025-00221-w.

[16] J. Li, D.J. Mooney, Designing hydrogels for controlled drug delivery, Nat Rev Mater 1 (2016) https://doi.org/10.1038/natrevmats.2016.71.

[17] K. Yue, G. Trujillo-de Santiago, M.M. Alvarez, A. Tamayol, N. Annabi, A. Khademhosseini, Synthesis, properties, and biomedical applications of gelatin methacryloyl (GelMA) hydrogels, Biomaterials 73 (2015) 254-271. https://doi.org/10.1016/j.biomaterials.2015.08.045.

[18] J.W. Nichol, S.T. Koshy, H. Bae, C.M. Hwang, S. Yamanlar, A. Khademhosseini, Cell-laden microengineered gelatin methacrylate hydrogels, Biomaterials 31 (2010) 5536-5544. https://doi.org/10.1016/j.biomaterials.2010.03.064.

[19] D. Loessner, C. Meinert, E. Kaemmerer, L.C. Martine, K. Yue, P.A. Levett, T.J. Klein, F.P. Melchels, A. Khademhosseini, D.W. Hutmacher, Functionalization, preparation and use of cell-laden gelatin methacryloyl-based hydrogels as modular tissue culture platforms, Nat Protoc 11 (2016) 727-746. https://doi.org/10.1038/nprot.2016.037.

[20] F. Cheng, L. Xu, X. Zhang, J. He, Y. Huang, H. Li, Generation of a photothermally responsive antimicrobial, bioadhesive gelatin methacryloyl (GelMA) based hydrogel through 3D printing for infectious wound healing, Int J Biol Macromol 260 (2024) 129372. https://doi.org/10.1016/j.ijbiomac.2024.129372.

[21] A.I. Van Den Bulcke, B. Bogdanov, N. De Rooze, E.H. Schacht, M. Cornelissen, H. Berghmans, Structural and rheological properties of methacrylamide modified gelatin hydrogels, Biomacromolecules 1 (2000) 31-38. https://doi.org/10.1021/bm990017d.

[22] M.C. Koetting, J.T. Peters, S.D. Steichen, N.A. Peppas, Stimulus-responsive hydrogels: Theory, modern advances, and applications, Mater Sci Eng R Rep 93 (2015) 1-49. https://doi.org/10.1016/j.mser.2015.04.001.

[23] H.G. Schild, Poly(N-isopropylacrylamide): experiment, theory and application, Progress in Polymer Science 17 (1992) 163-249. https://doi.org/10.1016/0079-6700(92)90023-r.

[24] A. Halperin, M. Kroger, F.M. Winnik, Poly(N-isopropylacrylamide) Phase Diagrams: Fifty Years of Research, Angew Chem Int Ed Engl 54 (2015) 15342-15367. https://doi.org/10.1002/anie.201506663.

[25] R. Pelton, Temperature-sensitive aqueous microgels, Adv Colloid Interface Sci 85 (2000) 1-33. https://doi.org/10.1016/s0001-8686(99)00023-8.

[26] Z. Li, D. Sun, J. Yang, S. Shang, L. Wang, H. Li, H. Zhang, R. Wang, H. Lan, X. Zhu, 3D printed heterogeneous bilayer temperature-responsive hydrogel with multi-curvature deformation, Polymer 296 (2024) https://doi.org/10.1016/j.polymer.2024.126701.

[27] Y. Ding, H. Ma, Z. Ji, D. Wei, H. Shang, L. Liu, N. Qiao, Preparation and properties of konjac glucomannan/P(N-isopropylacrylamide-crotonic acid) hydrogel, Polymer 340 (2025) https://doi.org/10.1016/j.polymer.2025.129181.

[28] Y.-Q. Liu, H.-Y. Guo, C.-Y. Hu, X. Xu, A novel dual pH- and temperature-responsive poly (N-isopropylacrylamide)/polyacrylamide/calcium alginate hydrogel with robust mechanical performance and biocompatibility for sustainable drug release, Polymer 327 (2025) https://doi.org/10.1016/j.polymer.2025.128386.

[29] Y. Shen, Y. Zhao, M. Tian, Y. Zhao, W. Yang, X. Zheng, W. Zhai, H. Liu, Multifunctional highly stretchable hydrogel with dual strain/temperature sensing for cardiac rehabilitation training, Polymer 335 (2025) https://doi.org/10.1016/j.polymer.2025.128803.

[30] J. Chen, C. Ning, Z. Zhou, P. Yu, Y. Zhu, G. Tan, C. Mao, Nanomaterials as photothermal therapeutic agents, Prog Mater Sci 99 (2019) 1-26. https://doi.org/10.1016/j.pmatsci.2018.07.005.

[31] S.Y. Tee, E. Ye, C.P. Teng, Y. Tanaka, K.Y. Tang, K.Y. Win, M.Y. Han, Advances in photothermal nanomaterials for biomedical, environmental and energy applications, Nanoscale 13 (2021) 14268-14286. https://doi.org/10.1039/d1nr04197e

[32] Y. Chen, L. Chang, Z. Zhang, M. Zhou, Y. Gao, Y. Wang, Y. Liu, J. Qin,. Biodegradable pectin-based thermo-responsive composite GO/hydrogel with mussel inspired tissue adhesion for NIR enhanced burn wound healing, Chemical Engineering Journal 480 (2024) https://doi.org/10.1016/j.cej.2023.148067.

[33] X. Huang, M.A. El-Sayed, Gold nanoparticles: Optical properties and implementations in cancer diagnosis and photothermal therapy, Journal of Advanced Research 1 (2010) 13-28. https://doi.org/10.1016/j.jare.2010.02.002.

[34] G. Fu, W. Liu, S. Feng, X. Yue, Prussian blue nanoparticles operate as a new generation of photothermal ablation agents for cancer therapy, Chem Commun (Camb) 48 (2012) 11567-11569. https://doi.org/10.1039/c2cc36456e.

[35] G. Dacarro, A. Taglietti, P. Pallavicini, Prussian Blue Nanoparticles as a Versatile Photothermal Tool, Molecules 23 (2018) https://doi.org/10.3390/molecules23061414.

[36] T. Pelluau, T. Brossier, M. Habib, S. Sene, G. Félix, J. Larionova, S. Blanquer, Y. Guari, 4D Printing Nanocomposite Hydrogel Based on PNIPAM and Prussian Blue Nanoparticles Using Stereolithography, Macromol. Mater. Eng. 309 (2023) https://doi.org/10.1002/mame.202300305.

[37] G. Ju, J. Tang, Q. Cheng, C. Wang, R. Liang, G. Sun, Tough, adhesive and thermosensitive PNIPAM/CNS hydrogel synthesized by tiny nanoparticles cross-linking, Polymer 308 (2024) https://doi.org/10.1016/j.polymer.2024.127355.

[38] C. Yi, Y. Yang, B. Liu, J. He, Z. Nie, Polymer-guided assembly of inorganic nanoparticles, Chem Soc Rev 49 (2020) 465-508. https://doi.org/10.1039/c9cs00725c.

[39] N. Jouault, D. Lee, D. Zhao, S.K. Kumar, Block-copolymer-mediated nanoparticle dispersion and assembly in polymer nanocomposites, Adv Mater 26 (2014) 4031-4036. https://doi.org/10.1002/adma.201305641.

[40] Y. Sui, Y. Cui, X. Meng, Q. Zhou, Research progress on the correlation between properties of nanoparticles and their dispersion states in polymer matrix, Journal of Applied Polymer Science 139 (2021) https://doi.org/10.1002/app.52096.

[41] S. Kango, S. Kalia, A. Celli, J. Njuguna, Y. Habibi, R. Kumar, Surface modification of inorganic nanoparticles for development of organic–inorganic nanocomposites—A review, Progress in Polymer Science 38 (2013) 1232-1261. https://doi.org/10.1016/j.progpolymsci.2013.02.003.

[42] G. Forte, A. Grassi, G. Marletta, Molecular modeling of oligopeptide adsorption onto functionalized quartz surfaces, J Phys Chem B 111 (2007) 11237-11243. https://doi.org/10.1021/jp068803h.

[43] C. Satriano, M.E. Fragalà, G. Forte, A.M. Santoro, D. La Mendola, B. Kasemo, Surface adsorption of fibronectin-derived peptide fragments: the influence of electrostatics and hydrophobicity for endothelial cells adhesion, Soft Matter 8 (2012) 53-56. https://doi.org/10.1039/c1sm06655b.

[44] H. Ejima, J.J. Richardson, K. Liang, J.P. Best, M.P. van Koeverden, G.K. Such, J. Cui, F. Caruso, One-step assembly of coordination complexes for versatile film and particle engineering, Science 341 (2013) 154-157. https://doi.org/10.1126/science.1237265.

[45] T.S. Sileika, D.G. Barrett, R. Zhang, K.H. Lau, P.B. Messersmith, Colorless multifunctional coatings inspired by polyphenols found in tea, chocolate, and wine, Angew Chem Int Ed Engl 52 (2013) 10766-10770. https://doi.org/10.1002/anie.201304922.

[46] D.K. Roper, W. Ahn, M. Hoepfner, Microscale Heat Transfer Transduced by Surface Plasmon Resonant Gold Nanoparticles, J. Phys. Chem. C 111 (2007) 3636-3641. https://doi.org/10.1021/jp064341w.

[47] X. Liu, B. Li, F. Fu, K. Xu, R. Zou, Q. Wang, B. Zhang, Z. Chen, J. Hu, Facile synthesis of biocompatible cysteine-coated CuS nanoparticles with high photothermal conversion efficiency for cancer therapy, Dalton Trans 43 (2014) 11709-11715. https://doi.org/10.1039/c4dt00424h.

[48] G. Li, S. Liu, Y. Chen, J. Zhao, H. Xu, J. Weng, F. Yu, A. Xiong, A. Udduttula, D. Wang, P. Liu, Y. Chen, H. Zeng, An injectable liposome-anchored teriparatide incorporated gallic acid-grafted gelatin hydrogel for osteoarthritis treatment, Nat Commun 14 (2023) 3159. https://doi.org/10.1038/s41467-023-38597-0.

[49] Y. Wu, S. Zhao, J. Wang, Y. Chen, H. Li, J.P. Li, Y. Kan, T. Zhang, Methods for determining the structure and physicochemical properties of hyaluronic acid and its derivatives: A review, Int J Biol Macromol 282 (2024) 137603. https://doi.org/10.1016/j.ijbiomac.2024.137603.

[50] Z. Qiao, L. Tran, J. Parks, Y. Zhao, N. Hai, Y. Zhong, H.F. Ji, Highly stretchable gelatin‐polyacrylamide hydrogel for potential transdermal drug release, Nano Select 2 (2020) 107-115. https://doi.org/10.1002/nano.202000087.

[51] P.L. Ritger, N.A. Peppas, A simple equation for description of solute release I. Fickian and non-fickian release from non-swellable devices in the form of slabs, spheres, cylinders or discs, J. Control. Release 5 (1987) 23-36. https://doi.org/10.1016/0168-3659(87)90034-4.

[52] R. Ye, Z. Zhu, T. Gu, D. Cao, K. Jiang, Q. Dai, K. Xing, Y. Jiang, S. Zhou, P. Cai, D.T. Leong, M. Yu, J. Song, Neutrophil extracellular traps-inspired DNA hydrogel for wound hemostatic adjuvant, Nat Commun 15 (2024) 5557. https://doi.org/10.1038/s41467-024-49933-3.

Supplementary Files

This is a list of supplementary files associated with this preprint. Click to download.

- SupportingInformation.docx